

## Localization and characterization of cracks in clay-rocks using frequency and time-domain induced polarization

G. Okay<sup>1,2</sup>, P. Cosenza<sup>3</sup>, A. Ghorbani<sup>4</sup>, C. Camerlynck<sup>1</sup>, J. Cabrera<sup>2</sup>,  
N. Florsch<sup>1,5</sup> and A. Revil<sup>6,7,\*</sup>

<sup>1</sup>UMR 7619 Sisyphé, Université de Pierre et Marie Curie, case courrier 105, Tour 56–46, 3ème étage, 4 Place Jussieu, 75252 Paris, France,

<sup>2</sup>French Institute of Radioprotection and Nuclear Safety, PO. Box 17, 92262 Fontenay-aux-Roses, France, <sup>3</sup>Université de Poitiers,

Laboratoire HydrASA, UMR CNRS 6269, ENSIP, Université de Poitiers, Bâtiment B1, 1 rue Marcel Doré, 86022 Poitiers Cedex, France,

<sup>4</sup>Department of Mining and Metallurgy, Yazd University, Safaieh, Pejoobesh Street, 89195–741 Yazd, Iran, <sup>5</sup>UMI 209 UMMISCO, Institut de Recherche pour le Développement, Paris, France, <sup>6</sup>Colorado School of Mines, Department of Geophysics, 1500 Illinois Street, Golden, CO 80401, USA and <sup>7</sup>ISTerre, CNRS, UMR CNRS 5275, Université de Savoie, 73376 Le Bourget du Lac Cedex, France

Received March 2011, revision accepted August 2011

### ABSTRACT

Induced polarization (IP) is a geophysical method that is potentially sensitive to the presence of cracks in porous rocks and therefore to damage. We performed time-domain and frequency domain IP measurements at the Tournemire Underground Research Laboratory (URL, Aveyron, France) in areas where different types of cracks are observed. These cracks correspond to both tectonic fractures and new cracks associated with stress release and desiccation resulting from the excavation of a gallery. These measurements were performed both in eastern and northern galleries of the test site. The eastern gallery was excavated in 1996 while the northern gallery was excavated recently in 2008. This gives us the opportunity to study the electrical characteristics of the excavation damaged zone surrounding the galleries with respect to the age of the excavation. Longitudinal profiles were performed along the floor of the galleries with 48 Cu/CuSO<sub>4</sub> electrodes separated by a distance of 20 cm. Chargeability and resistivity were inverted using a Gauss-Newton iterative approach assuming an isotropic heterogeneous clay-rock material. The resulting IP tomograms show a correlation between high values of chargeability and the presence of calcite-filled tectonic fractures. X-ray analysis indicates that the presence of pyrite in these fractures is a potential source of the observed IP signals. The cracks associated with the mechanical damage of the formation exhibit low values of chargeability, on the same order of magnitude than the chargeability of the clay-rock matrix and are therefore hardly observable. A smaller IP response associated with the presence of these cracks is observed in the older gallery and this observation is qualitatively related to the desaturation process associated with these cracks. In a specific area of one of the galleries, the presence of calcareous nodules is observed to be an important source of anomalous chargeability. This signature seems to be associated with the presence of pyrite.

**Key words:** Induced polarization, Desiccation.

---

\*E-mail: arevil@mines.edu

## 1 INTRODUCTION

Historically, the induced polarization (IP) method has been used for the exploration of ore bodies and oil reservoirs (Pelton *et al.* 1978; Nelson and Van Voorhis 1983, Seigel *et al.* 2007). Ore bodies are usually associated with large values of the phase lag between the current and the voltage ( $>10$  mrad, see Marshall and Madden 1959; Pelton *et al.* 1978). More recently and thanks to the increase of the sensitivity of field equipments (sensitivity less than 1 mrad for the phase), the IP method has been used for environmental purposes. The reasons for this interest are multiple: 1) IP shows a sensitivity to parameters (specific surface area, grain size, pore size) that can be used to characterize the permeability of porous rocks (Börner, Schopper and Weller 1996; Sturrock, Lesmes and Morgan 1999; Revil and Florsch 2010), 2) IP is sensitive to change in the chemistry of pore water (Vaudelet *et al.* 2011a,b), 3) IP is sensitive to different types of contaminants (Olhoeft 1984, 1985, 1992; Vanhala, Soininen and Kukkonen 1992; Kemna, Binley and Slater 2004), 4) IP can be used to characterize clay materials (Weller and Börner 1996; Lesmes and Friedman 2005, Jougnot *et al.* 2010) and 5) IP is also sensitive to the presence of heterogeneities like cracks in rocks (Schwartz, Sen and Johnson 1989; Knight and Endres 1990; Kruschwitz and Yaramanci 2004).

However, despite the development of new 4D tomography algorithms (Karaoulis *et al.* 2011), the interpretation of induced polarization is complicated by the fact that several polarization mechanisms overlap in the frequency domain including electrical double layer polarization mechanisms occurring at the pore scale or at the grain scale plus Maxwell Wagner polarization due to the discontinuity of the displacement current at the boundary between the different phases of a porous rock (Sen, Chew and Wilkinson 1984; Knight and Endres 1990; Leroy *et al.* 2008; Leroy and Revil 2009; Jougnot *et al.* 2010; Schmutz *et al.* 2010). In addition, the presence of pyrite can be responsible for a strong IP response.

The recent interest in studying the transport properties of clay materials and especially clay-rocks, is related to their usefulness to confine different types of wastes. Indeed, clay-rich materials are indeed characterized by very low permeabilities (usually smaller than  $10^{-19}$  m<sup>2</sup>) and high specific surface areas (from 5–40 m<sup>2</sup>/g for kaolinite up to 800 m<sup>2</sup>/g for smectite). In Europe, research works have been performed to study the confining properties of *in situ* clay-rocks in underground laboratories. One open question remains – the characterization of the damage due to the excavation of galleries of *in situ* clay-rich formations upon their transport properties, es-

pecially permeability (Blümling *et al.* 2007) and the usefulness of the geophysical method to monitor the evolution of damage over time (cracking and healing processes). The creation and extension of the so-called excavation damaged zone around the galleries are controlled by 1) the initial stress field, 2) the distribution of the mechanical properties of the material, 3) the permeability distribution, 4) the geometry of the gallery, 5) the relative humidity of the air in the gallery and 6) the presence of pre-existing natural fractures (Bossart *et al.* 2002; Tsang, Bernier and Davies 2005; Matray, Savoye and Cabrera 2007; Blümling *et al.* 2007).

In fractured and unsaturated clay materials, IP is sensitive to the electrical properties of the background clay matrix, to the saturation of the water phase and to the density and orientation of cracks (Nover, Heikamp and Freund 2000; Kruschwitz and Yaramanci 2004; Schmutz *et al.* 2011). To the best of our knowledge, no geophysical investigations have been performed to date to recognize different types of cracks in these types of environment (tectonic *versus* recent cracks associated with damage) using both time-domain and frequency domain IP measurements. We have already conducted some laboratory works (Cosenza *et al.* 2007; 2008; Ghorbani *et al.* 2009; Jougnot *et al.* 2010) on this subject that are discussed below in Section 5. These works have demonstrated that new cracks can change the chargeability of clay-rocks. In the present paper, we present a quantitative study in the field to test the ability of time-domain and frequency domain IP to detect cracks around the galleries of the Underground Research Laboratory (URL) test site of Tournemire (Aveyron, France), which is a well-characterized underground laboratory.

## 2 DESCRIPTION OF THE TEST SITE

### 2.1 Geological and mineralogical context

The Tournemire URL test site was chosen by the French Institute of Radioprotection and Nuclear Safety (IRSN) to perform research regarding the confining properties of low-porosity clay-rocks (Cabrera *et al.* 2001; Rejeb and Cabrera 2006; Gélis *et al.* 2010). Such type of fundamental work is important to characterize the ability of these rocks to confine radioactive wastes during their life-time. This site is located in southern France, in the western border of the Causses Basin. The general stratigraphy of the Tournemire massif is sub-horizontal (see Fig. 1) and comprises three major formations: i) the lower formations correspond to Hettangian, Sinemurian and Carixian age formations, ii) the intermediate formations (Domerian and Toarcian) correspond to marls and clay-rocks and iii) the

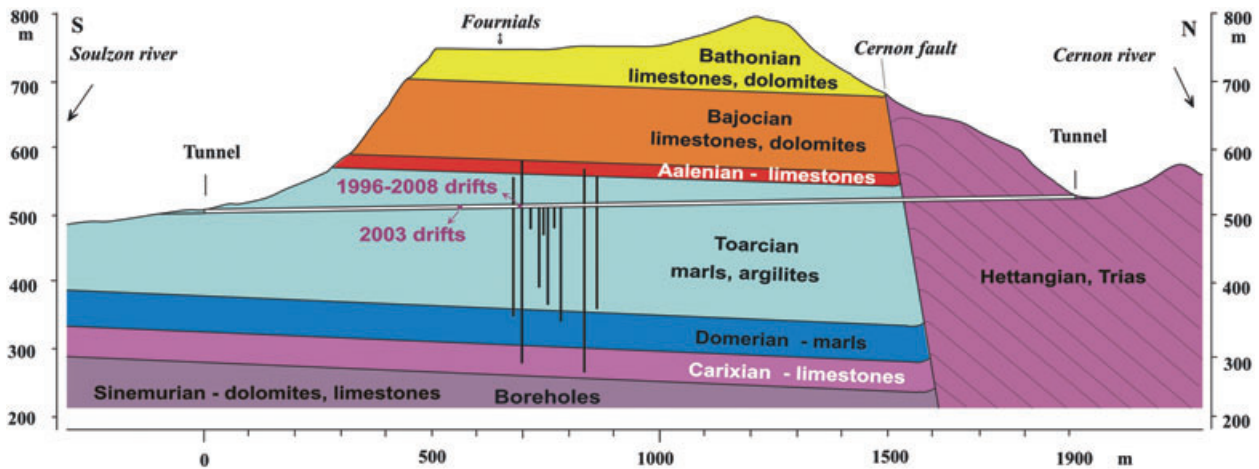


Figure 1 Geological cross section of the Tournemire experimental station. The tunnel is mainly drilled through the Toarcian clay-rock formation.

upper formations (Upper Aalenian, Bajocian and Bathonian) consist of limestones and dolomites.

The main formation of interest at this site is the upper Toarcian clay-rock formation (250 m thick). This clay-rock is a good analogue of the Callovo-Oxfordian clay-rock in the Paris Basin that is considered to be a potential host for the long-term storage of nuclear wastes in France. Six galleries plus an old railway tunnel are used to study the Toarcian formation (see Cabrera *et al.* 2001 and Fig. 2). The clay fraction of the upper Toarcian formation (shown in Fig. 3) ranges from 20–50% of the bulk rock in volume. It is mainly composed of illite (5–15% weight fraction), illite/smectite mixed-layer minerals (5–10% with a relative proportion of smectite of about 10%), chlorite (1–5%) and kaolinite (15–20%). This formation also contains 10–20% of quartz grains (weight fraction), 10–40% of carbonates (mainly composed of calcite with

traces of dolomite and siderite) and 2–9% (in weight) of pyrite disseminated in the clay matrix spreading until 160 m deep from the tunnel (Cabrera *et al.* 2001; Savoye *et al.* 2001, 2006).

Three campaigns of field measurements were performed in June 2008, June 2009 and February 2010 in two distinct galleries of the Tournemire URL test site: the East gallery and the North gallery (Fig. 4a,b). The East gallery was excavated in 1996 and the North gallery was excavated more recently in 2008 (Fig. 2). These are described in more detail in the next two sub-sections.

## 2.2 East gallery

IP measurements were first performed in the East gallery, which was excavated in 1996 (Fig. 3). Two reasons guided this choice: 1) the excavation damaged zone is less developed in this gallery with respect to the excavation damaged zone of the old railway tunnel, itself excavated in 1882 (Cabrera *et al.* 2001; Contrucci *et al.* 2007) and 2) the clay-rock can directly be reached from the gallery wall since no concrete lining exists on the surface of the gallery. The cross-section of this gallery has a horseshoe shape (Fig. 4a) with a height of 3.7 m and a width along the floor of the gallery of 4 m. Its direction is east-west with a length of 30 m (Fig. 2). Its mechanical stability is ensured by steel supports regularly spaced every 2 metres (Fig. 4a).

Two families of cracks can be observed by visual inspection along the walls and the floor of this gallery. The first family of cracks (millimetre-scale width and metre-scale extension) corresponds to sub-vertical fractures, called ‘new fractures’ below (Fig. 3a). These fractures occurred after the drilling of

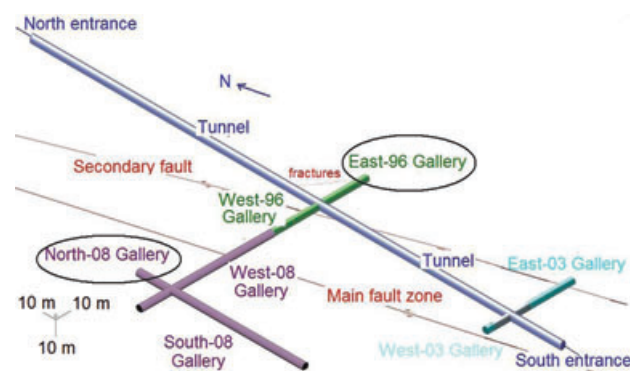
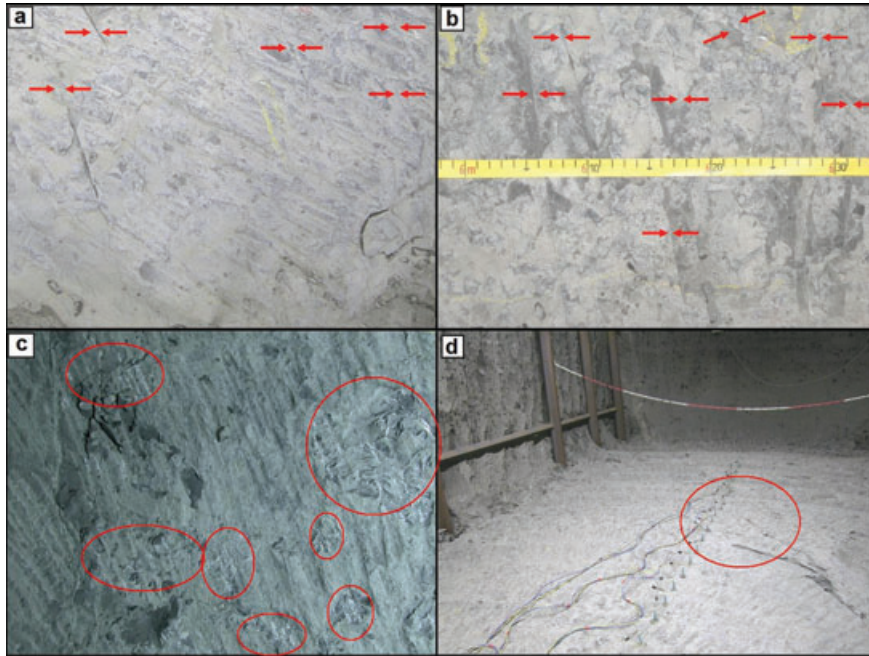


Figure 2 Position of the galleries at the experimental site. The prospected areas correspond to the two bold areas (East-96 gallery and North-08 Gallery).



**Figure 3** Heterogeneities in the galleries. (a) Picture showing the recently formed new cracks in the East gallery. (b) Picture showing the calcite-filled tectonic fractures in the Esat gallery (at around 6 m from the beginning of the electrical profile along the floor). (c) Picture showing the calcareous nodules in the North gallery. (d) Picture showing the tectonic fracture on the floor in the North gallery.

the gallery. They result from the release of the mechanical stress associated with the drilling of the gallery (Rejeb and Cabrera 2006). The second family of cracks corresponds to calcite-filled tectonic fractures. We will see later that these calcite-filled fractures contain also some pyrite. They can be observed along the floor of the gallery (see Fig. 3b). These fractures have roughly the same dimensions as the new fractures mentioned above (mm-scale width and m-scale extension). These fractures are of geological nature and associated with the tectonic history of the clay-rock formation. They are termed ‘tectonic fractures’ below.

### 2.3 North gallery

Our goals in performing IP measurements in the North gallery were the following: 1) studying the excavation damaged zone characteristics in terms of heterogeneities of a more recently drilled gallery (drilling occurred in May 2008) and 2) comparing IP characteristics between this gallery and the East gallery, which have different ages of excavation. The advantage of the North gallery is that its geological context is similar to the East gallery (1996) (both new fractures and calcite-filled tectonic fractures are observed on the floor). In addition, calcareous nodules are also observed in the North gallery (none in the East gallery) pervasively into the clay-rock on the lower part

of the walls and on the floor (see Fig. 3c). These nodules will have a non-negligible role on the IP tomograms.

The shape of the cross-section of the North gallery is a horseshoe with a height of 3.7 m and a width along the floor of 4 m (Fig. 4b). This corresponds to the same dimensions as for the East gallery. This gallery is oriented north-south with a length of 20 m (Fig. 2). There is no concrete layer on the floor except for the first 7 m from the entry of the drift. The East and North galleries have been excavated with the same drilling method using a cutterhead dredge.

## 3 INDUCED POLARIZATION MEASUREMENTS: METHODOLOGY

Both time-domain (TD) and frequency domain (also called spectral induced polarization (SIP) in a number of publications) induced polarization measurements can be performed in the field (e.g., Dahlin, Leroux and Nissen 2002; Ghorbani *et al.* 2007).

### 3.1 Time-domain induced polarization measurements

Time-domain induced polarization (IP) measurements are performed by applying a square electric current between two electrodes (A and B) to the rock and measuring the voltage after

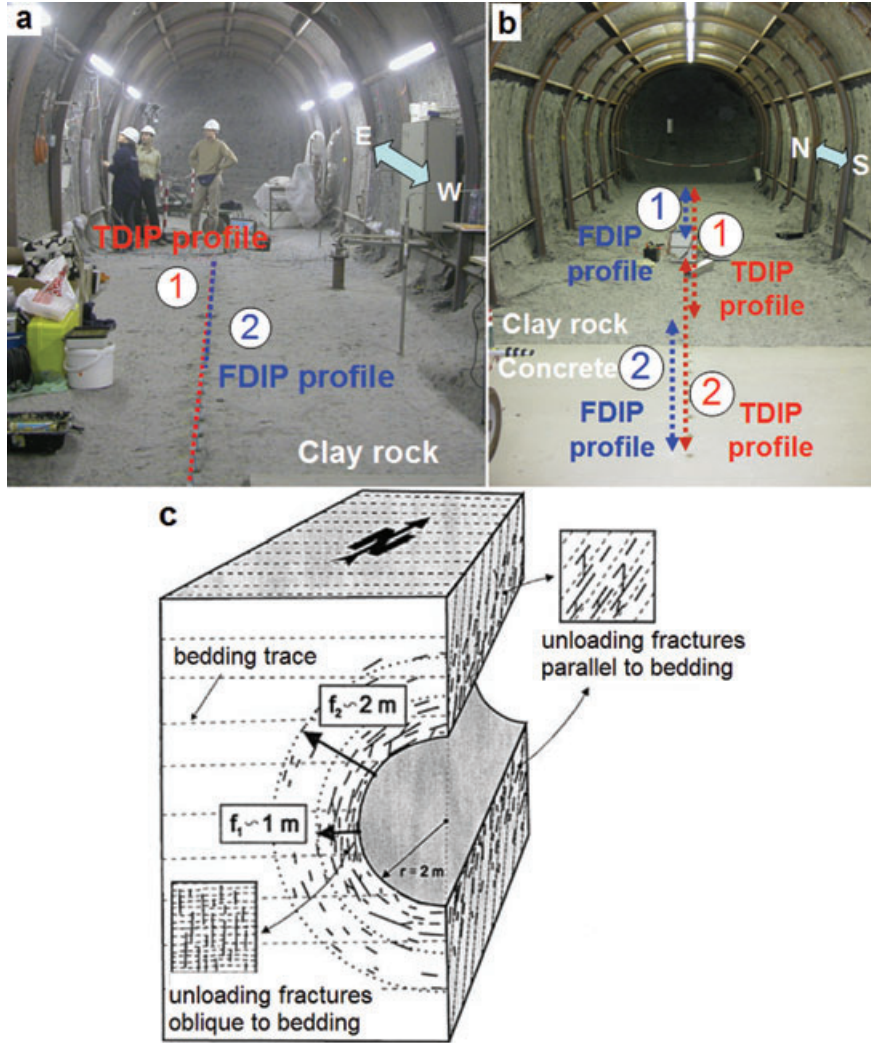


**Figure 4** Position of the time-domain (TDIP) and frequency-domain (FDIP) IP longitudinal profiles along the floor in (a) the East gallery and (b) the North Gallery. (c) Sketch of the EDZ. at the laboratory of Mont Terri showing the new fractures associated with the stress release associated with the gallery.

the current is turned off. The decay of the difference of the electrical potential between a pair of potential electrodes (M and N),  $V_s$ , is measured over time. The apparent chargeability (expressed in mV/V) is given as,

$$M_a = \frac{1}{V_p \Delta t} \int_{t_1}^{t_2} V_s dt, \quad (1)$$

where the time-dependent residual voltage  $V_s$  (expressed in mV) is integrated over a time window defined between the times  $t_1$  and  $t_2$  after the applied current is turned off between A and B. The voltage  $V_p$  is the measured voltage between M and N just before the current is turned off (primary voltage,

expressed in V). The time  $\Delta t = t_2 - t_1$  defines the duration of the time window. We use three different durations for the current injection, 1, 2 and 4 s with Syscal Pro from Iris Instrument. For the measurement of the voltage decay after the current electrodes are shut down, we use a Cole-Cole discretization with 20 windows. For a 4 s current injection, the time at which the decaying secondary voltage is measured corresponds to the following series: 20, 40, 50, 60, 70, 80, 90, 100, 110, 120, 140, 160, 180, 200, 220, 250, 280, 320, 380, 450 and 530 ms. Therefore in this case, we have  $\Delta t = 510\text{ ms}$  if all the decay window is used. For a 1 s current injection, we have  $t_1 = 10\text{ ms}$ ,  $t_2 = 90\text{ ms}$  and therefore  $\Delta t = 80\text{ ms}$ . For

a 2 s current injection, we have  $t_1 = 20$  ms,  $t_2 = 200$  ms and therefore  $\Delta t = 180$  ms. Physically, the chargeability describes the ability of a porous material to store reversibly electrical charges.

Time-domain IP measurements were performed in both galleries with the Syscal Pro impedance meter from Iris instruments (<http://www.iris-instruments.com>). Longitudinal profiles were chosen along the axis of the galleries. Measurements were performed along one profile in the East gallery and two profiles in the North gallery. The length of these profiles is 9.40 m. They comprise 48 electrodes with a spacing of 20 cm. This spacing has been chosen in order to ensure sufficient electrical resolution to image the entire thickness of the damaged zone. Using small drill-holes, this thickness was estimated to be on the order of 0.7–1.1 m (Contrucci *et al.* 2007). To install the electrodes on these profiles, drillings were first performed with holes  $12 \pm 1$  mm in diameter and with a depth of  $5.0 \pm 0.1$  cm. Before putting the electrodes in these holes, wet bentonite was injected to ensure a good electrical contact between the clay-rock and the non-polarizing Cu/CuSO<sub>4</sub> electrodes (6 mm in diameter). These electrodes were used both as current and potential electrodes. Some of these holes were also used for the frequency domain IP measurements.

### 3.2 Frequency domain induced polarization measurements

Frequency domain IP measurements were performed at different locations along the profiles where time-domain IP data were collected. For the frequency domain measurements, the same methodology as applied for time-domain measurements was used including the use of non-polarizing Cu/CuSO<sub>4</sub> electrodes and wet bentonite. In the East gallery, frequency domain IP measurements were performed with the SIP FUCHS-II apparatus from Radic Research (<http://www.radic-research.homepage.t-online.de/default.html>). The SIP FUCHS-II can measure the complex resistivity from 1.43 mHz up to 12 kHz. In the case study reported below, we measure the complex resistivity over 7 decades in frequency from 4.5 mHz up to 12 kHz. It consists in two remote units that record the current  $I^*(\omega)$  (between electrodes A and B) and the difference of voltage between the two electrodes M and N,  $U^*(\omega)$  and the phase lag between the current and the voltage difference.

The impedance  $Z^*$  is defined as (Pelton, Sill and Smith 1983):

$$Z^*(\omega) = \frac{U^*(\omega)}{I^*(\omega)} = |Z^*(\omega)| e^{i\varphi(\omega)}, \quad (2)$$

where  $i^2 = -1$  ( $i$  is the pure imaginary number) and  $|Z^*(\omega)|$  and  $\varphi(\omega)$  are the amplitude of the impedance and the phase lag between the current and the voltage, respectively. To measure the whole spectrum of frequencies, the SIP FUCHS-II apparatus starts with the highest frequency, 12 kHz and  $N = 18$  in our case ( $N = 24$  in the general case), other decreasing frequencies are obtained by the following division:  $12 \text{ kHz}/2^N$ . Optic fibres were used to minimize the electromagnetic coupling between the ground and the cables of the apparatus. The error on the phase lag was about  $\pm 1$  mrad on the measurements above 6 kHz. For lower frequencies, the accuracy on the phase lag was better than  $\pm 0.5$  mrad. This is a typical error level for the SIP FUCHS-II apparatus operating in normal field conditions (Weller, Seichter and Kampke 1996; Binley *et al.* 2005).

To limit the acquisition time (2 hours for the whole spectrum for one data point), we considered two solutions: i) instead of performing frequency domain IP measurements on the entire profile investigated by time-domain IP data (9.40 m in length), the sections characterized by anomalous chargeability were prioritized. The selected profile started at  $x = 2.6$  m from the beginning of the time-domain IP profile and was  $\sim 5$  m long (Fig. 4a) and ii) the frequency range used in the acquisition was limited from  $f = 366$  mHz to 12 kHz. Only for the anomalous areas observed in the time-domain IP tomograms was the lower bound of the investigated frequencies lowered to 46 mHz. The frequency domain IP acquisitions were performed with the Wenner array only. Five different spacing  $a$  were used during the acquisition ( $a = 20$  cm, 40 cm, 60 cm, 80 cm and 100 cm). These distances were used to define the geometrical factors used to convert the impedances to resistivities.

In the North gallery, frequency domain IP measurements were performed with a prototype developed at the UMR 7619 Sisyphé Research Laboratory of Pierre Marie Curie University. Our goal was to test the capacity of such a prototype for *in situ* characterization. This device can work in the frequency range  $f \in [1.86 \text{ mHz}, 31.25 \text{ kHz}]$  (therefore overlapping and extending the frequency range investigated by the SIP FUCHS-II apparatus). The transmitter and receiver of the prototype were separated by a distance of 1 m. This system allows a higher control of the output voltage (up to 200 V) by comparison with the SIP FUCHS-II apparatus (limited to 10 V). The measurements were performed on two different profiles used for the time-domain IP acquisition. The first one started from the beginning of the time-domain IP acquisition profile and ends in 4 m. This zone was relatively less affected by the presence of the calcareous nodules (according to visual

observations and time-domain IP data). The second frequency domain IP profile (length of 6 m) was chosen at the end of the time-domain profile (Fig. 4b). The frequency domain IP acquisitions were performed with the Wenner-Schlumberger array only. Three different inter-electrode separations were used during the acquisition ( $n = 1$ ,  $a = 20$  cm;  $n = 2$ ,  $a = 20$  cm;  $n = 3$ ,  $a = 20$  cm; where  $a$  is the distance between potential electrodes M and N and  $n$  is multiplying coefficient of the distance between a current and potential electrode). The frequency range was limited from  $f = 0.2$  Hz to 7 kHz for an optimum acquisition time per measure ( $\sim 2$  minutes). Frequency domain sampling was logarithmic. From repeatability tests, the error on the measurements was on the order of 1 mrad for the higher frequencies ( $> 1$  kHz) and 0.4 mrad for the intermediate and low frequencies. We will see later in Section 5.3 that the pyrite present in the calcite-filled tectonic fractures should have a signature at few tens of Hertz to few hundreds of Hertz. Therefore the frequency domain IP tomograms are given at relatively high frequency.

#### 4 RESULTS

To display the results obtained in the two galleries, two kinds of representations may be used: 1) the raw data can be inverted to obtain tomograms assuming that the material is heterogeneous but isotropic and 2) spectra of IP parameters obtained through the analysis of the frequency domain IP data can be displayed. Regarding the first representation, both the resistivity and the chargeability can be displayed as tomograms. The spectral induced polarization data can be displayed as tomograms for the resistivity and the phase.

The inversion of the time and frequency domain IP data was performed with the software Res2DINV from GEOTOMO (Loke and Barker 1996) using a Gauss-Newton approach and the finite element approach to solve the forward problem. In addition to the inversion of the resistivity in both time and frequency domains, this software supports also the introduction of various types of IP data including i) (time-domain) chargeability and ii) the phase lag. IP values that are given in other units in the frequency domain are converted into chargeability values. The relevant conversion equations can be found in Kemna (2000), Nelson and Van Voorhis (1973) and Van Voorhis, Nelson and Drake (1973) and will not be repeated here. It is also important to understand the limitations of the present approach. The preferential orientation of the fractures and cracks implies that the clay-rock is not isotropic. In this situation, the complex resistivity should be described by a second-order symmetric tensor. While few recent works have

developed an inversion approach accounting for the tensorial nature of the resistivity (Kenkel, Hördt and Kemna 2011; Andreas Hördt, pers. comm. 2011) no code was accessible to us to perform the inversion of the full resistivity tensor. Therefore we considered that the material was isotropic as a first-order approximation. The inversion of the IP data is carried out as a perturbation of the resistivity model using a Tikhonov-type smoothness-constrained least square problem solved with the Gauss-Newton approach (see details in Tikhonov and Arsenin 1977; de Groot Hedlin 1990; Vauhkonen *et al.* 1998).

Regarding the East gallery, the tomograms based on the time-domain IP data are plotted in terms of inverted resistivity and chargeability distributions. For the spectral induced polarization data, the tomograms are plotted at the following frequencies  $f = 366$  mHz and 732 mHz. As shown below, these frequencies are close to the low-frequency polarization peak typically observed at 0.1–0.3 Hz. The distributions of the phase are shown on the tomograms. All the tomograms for the East gallery are based on the data performed with the Wenner and Wenner-Schlumberger arrays. Concerning the North gallery, we performed the same work. However, for the frequency domain IP data, the tomograms are plotted only at two distinct frequencies  $f = 7$  Hz and  $f = 61$  Hz. These frequencies are used to avoid electromagnetic coupling effects occurring usually above 1 kHz.

We will also display the IP parameters obtained from the spectral induced polarization data. We plot the magnitude of the resistivity  $|\rho^*|$  (in  $\Omega$  m) and the phase lag  $\varphi$  (in mrad) versus the frequency. We can also plot the in-phase (real) conductivity  $\sigma'$  and the out-of-phase (imaginary or quadrature) conductivity  $\sigma''$  (in S/m), both as a function of the frequency. Among these parameters, the phase lag  $\varphi$  defines the ratio of polarization to conduction,  $\sigma'' / \sigma'$  (Lesmes and Frye 2001; Slater and Lesmes 2002). In the following, we will present the spectra of the phase shift,  $\varphi$  and quadrature conductivity  $\sigma''$ .

##### 4.1 Detection of the calcite-filled fractures

The resistivity tomograms (Fig. 5) show clearly the presence of the extension of the excavation damaged zone. This zone corresponds to the high resistivity values ( $\sim 400$   $\Omega$  m) on the longitudinal profile of the Eastern gallery. Nevertheless, the resistivity tomograms do not allow distinguishing between the calcite-filled tectonic fractures and the newly opened cracks. However, time-domain and frequency domain IP tomograms (chargeability and phase) show clearly the positions of the calcite-filled fractures in Fig. 6 in agreement with the

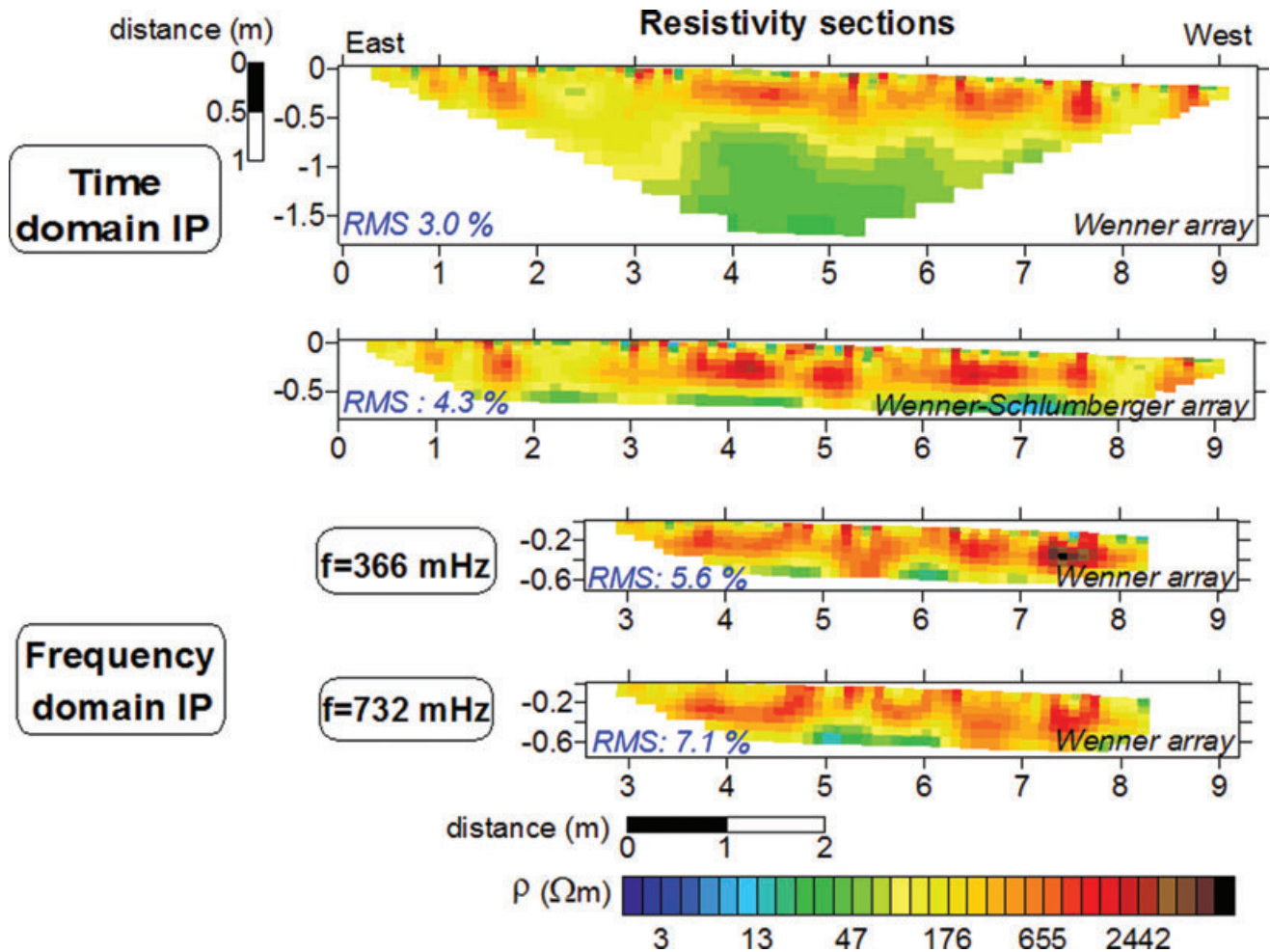


Figure 5 Inverted resistivity sections obtained from time and frequency-domain IP measurements (at  $f = 366$  mHz and  $f = 732$  mHz, respectively, Wenner and Wenner-Schlumberger arrays, iteration number: 4, East gallery). The acquisitions were performed in June 2008.

observations made along the floor of the galleries. Consequently, the observed polarization is associated with these fractures. The mechanism of polarization will be discussed below. The spectra of the phase lag and the quadrature conductivity indicate also the presence of anomalies that are consistent with the positions of the observed calcite-filled tectonic fractures. These fractures have a spectral signature showing a broad polarization peak (dispersion) in the low-frequency range (10 mHz to 1 Hz, see for instance Fig. 7).

The difficulty in interpreting IP measurements is to connect such a polarization peak to a specific mechanism. We will see that the underlying mechanism of the observed polarization may be related to the mineralogical content of the material filling the tectonic fractures. Indeed, pyrite is known to have a strong effect upon spectral induced polarization (e.g., Pelton *et al.* 1978; Wong 1979). Campbell, Horton and Beanlang

(2000) performed laboratory measurements on samples containing 2% of pyrite and they observed a phase peak at  $f = 1$  Hz. Bonin (1998), Boisson, Cabrera and De Windt (1996, 1997), De Windt, Cabrera and Boisson (1999) and Mathieu *et al.* (2000) showed that the calcite-filled fractures of the Tournemire test site also have some pyrite. Our analysis is showing that the size of the pyrite grain is typically in the range 0.1–1 mm. Peyaud *et al.* (2006) mentioned that the filling of most of the large-scale fractures consists of calcite veins with the presence of pyrite and sometimes barite. Because of the lack of prior knowledge about the amount of pyrite in the material filling these fractures, we performed also a mineralogical analysis of the filling material using the X-ray diffraction method. For this purpose, we use a sample of material filling the tectonic fracture characterized by high values of the chargeability at  $x = 6$  m on the electrical profile (Fig. 6). The

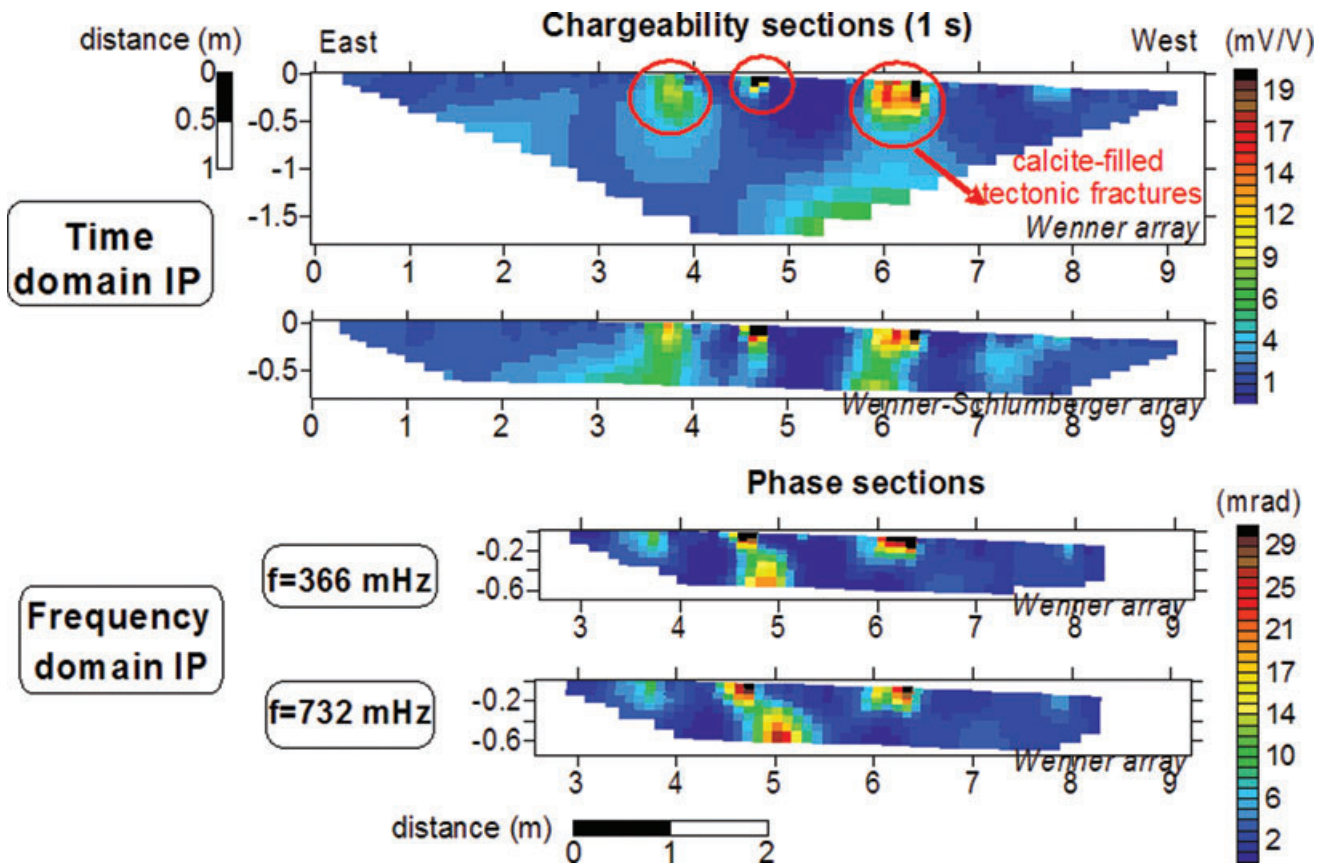


Figure 6 Inverted time-domain chargeability tomogram, phase from frequency-domain IP data ( $f = 366$  mHz, 732 mHz). We used the Wenner and Wenner-Schlumberger arrays in the East gallery for the time-domain induced polarization (error RMS is smaller than 1%, iteration number: 4) and the Wenner array for the frequency-domain induced polarization. The acquisitions were performed in June 2008.

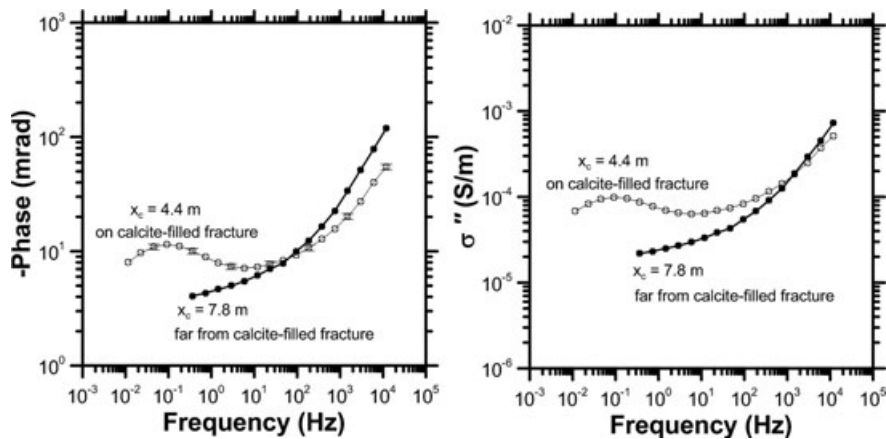


Figure 7 Phase and quadrature conductivity spectra of the longitudinal profile performed at the floor of the gallery at two distinct locations: (i) at the position of an observed calcite-filled fracture ( $\sim x_c = 4.4$  m) and (ii) far from this calcite-filled fracture (at position  $x_c = 7.8$  m) (see Figure 6) in the East gallery (Wenner- $\alpha$  array, electrode separation: 80 cm, apparatus: SIP FUCHS-II). An open question is related to the physical mechanism of the low-frequency relaxation in the case of the calcite-filled tectonic fractures and its possible relationship to the presence of pyrite in these fractures (see Table 1).

**Table 1** Mineralogical composition of the material filling the tectonic fractures according to the X-ray analysis (% in weight and volume)

Mineral	Carbonate matrix (weight%)	Crystallized veins (weight%)	Mass density ( $\text{kg m}^{-3}$ )	Carbonate Matrix (vol.%)	Crystallized veins (vol.%)
Calcite	40	73	2710	44	80
Quartz	24	10	2650	27	10
Pyrite	16	11	5010	8	6
Mica	13	3	2883	14	2
Kaolinite	7	Trace	2700	7	Trace
Chlorite	0	3	2900	0	2
Gypsum	Trace	Not detected	-	Not detected	Not detected

result of the X-ray diffraction analysis allows distinguishing three major minerals from the studied sample. First a carbonate matrix is detected with mainly calcite, silica and a significant amount of pyrite (16% in weight) (Table 1). This matrix is partially intersected by millimetre-scale veins made of crystallized minerals (0.1–1 mm in size) including pyrite. Table 1 represents the mineralogical composition of the material filling the tectonic fractures. Pyrite forms 11% (in weight) of the materials forming the crystallized veins. The presence of this pyrite both in the carbonate matrix filling the fractures and in the form of veins could therefore explain the polarization associated with the tectonic fractures in a clay-rich rock.

#### 4.2 New fractures

On the longitudinal profile of the East gallery, a visual inspection of the floor of the gallery shows the presence of new fractures with no filling and mineralization. However, contrary to the tectonic fractures existing on the same profile, the chargeability tomogram shows no or few evidences of these new fractures. Despite the fact that these fractures are only partially saturated, they do not have a clear IP signature below 1 kHz. To investigate in more detail the electrical response of these fractures, a small profile, far from the other heterogeneities, was performed in the East gallery in February 2010. This profile passes over a dense zone of new fractures (see details in Fig. 8a).

On this (longitudinal) profile located on the floor, time-domain IP measurements were performed with the Syscal Pro apparatus. We use 18 steel electrodes ( $3 \times 55$  mm) with a spacing of 10 cm. The resistivity and chargeability tomograms (for 1 s and 4 s injection times) are shown in Fig. 8(b). We observed

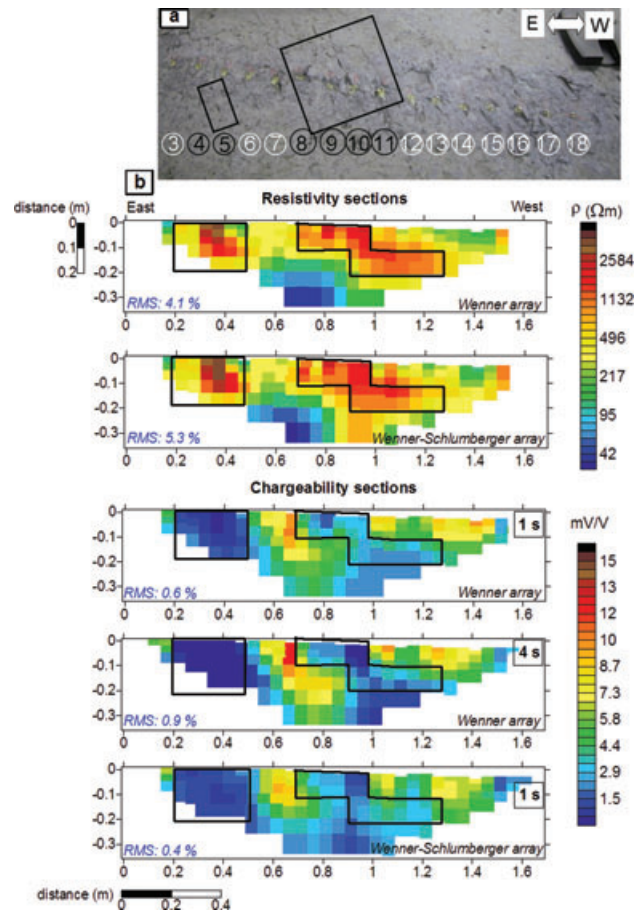


**Figure 8** (a) Picture of the profile showing the presence of the new cracks. (b) Inverted resistivity and chargeability sections (1 s and 4 s) using the Wenner and Wenner-Schlumberger arrays in the East gallery (iteration number: 4). The rectangles correspond to areas characterized by high resistivity and low chargeability and the numbers correspond to the electrodes. Acquisition performed on February 2010.

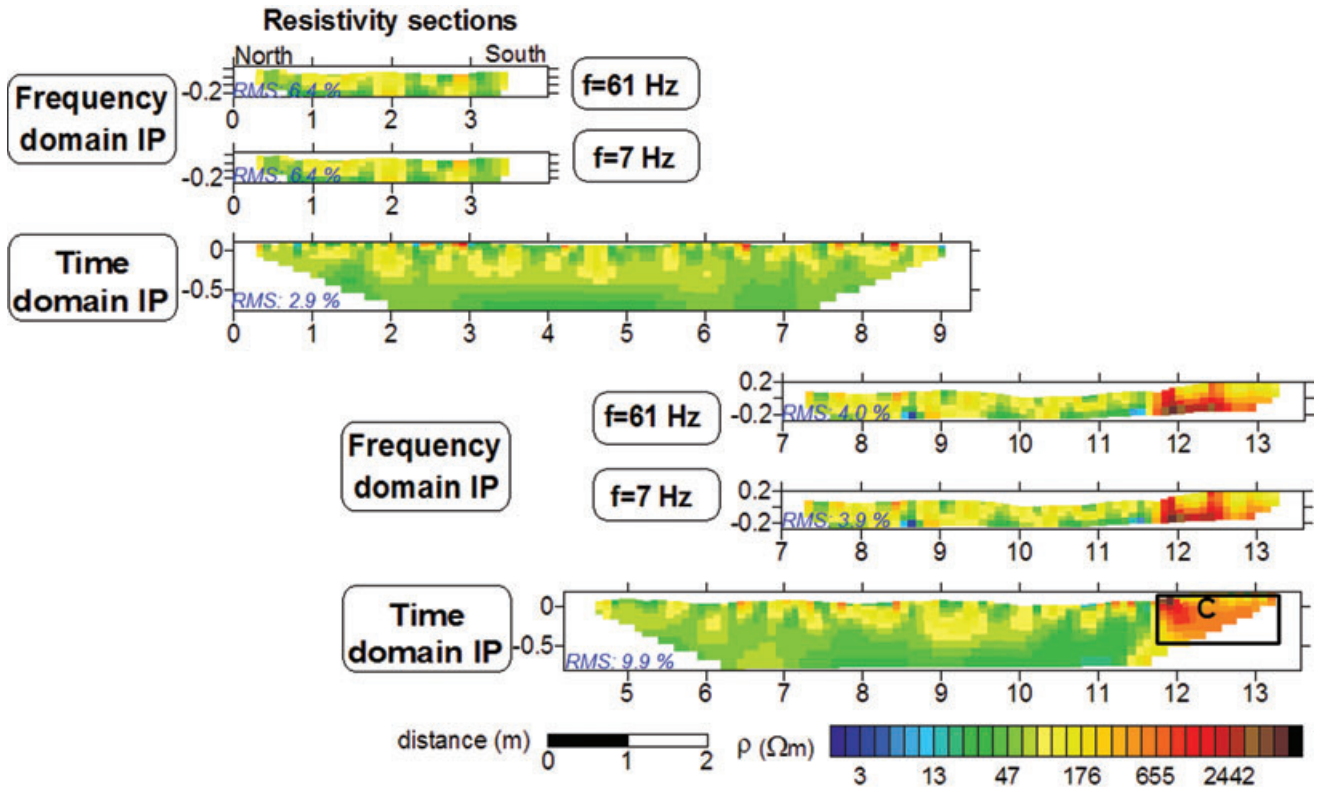


**Figure 9** Inverted resistivity sections obtained from time- and frequency-domain IP measurements ( $f = 7$  Hz and 61 Hz, Wenner-Schlumberger array, iteration number: 4) in the North gallery. The letter C indicates the concrete layer. The acquisition was performed in June 2009. The choice of the two frequencies represent a trade-off between the duration of the acquisition and the need to show low-frequency data for which there is a distinct polarization associated with the presence of the fractures.

two areas characterized by very low values of chargeability ( $<4$  mV/V) (areas in blue underlined by rectangles in Fig. 8b). These areas correspond also to high resistivity anomalies on the resistivity tomograms (in red underlined by rectangles in Fig. 8b). These resistivity and IP anomalies are correlated with areas of high density of new fractures. We believe that the reason for the high resistivity values is related to the drying of the clay-rock through these cracks. Indeed, desaturation occurs faster in areas where the pores are large and the capillary pressure is smaller. Moreover, the desaturation process is reinforced by the natural ventilation of the tunnel. Desaturation of the damaged zone leads to higher resistivities and higher phases because the phase is proportional to the resistivity (see Jougnot *et al.* 2010). For the remaining part of the profile, there are less favourable conditions preventing the material to desaturate. This explains the slightly higher chargeabilities for these sections. In conclusion, we suggest that chargeability associated with the new fractures is dependent on the saturation state of the material as modelled by Jougnot *et al.* (2010)

and discussed below in Section 5. Higher damages (expressed by macroscopic cracks) correspond therefore to lower chargeabilities through the effect of desaturation. This is also a new finding.

#### 4.3 Induced polarization signature of the calcareous nodules

The chargeability tomogram resulting from the acquisition performed in June 2009, in the North gallery, shows changes in the values of the chargeability from 1–15 mV/V for the first acquisition profile N°1 to 0–24 mV/V for the second acquisition profile N°2 (Fig. 10). These tomograms were plotted with chargeability values comprised between 0–20 mV/V only to better evidence the small anomalies. To interpret these results, the anomalous chargeability zones are indicated by letters in Fig. 10. The obtained chargeability anomalies are divided into three types from direct observations through microdrilling: A stands for the tectonic fracture, B for the calcareous nodules and C for the concrete layer (Fig. 10).

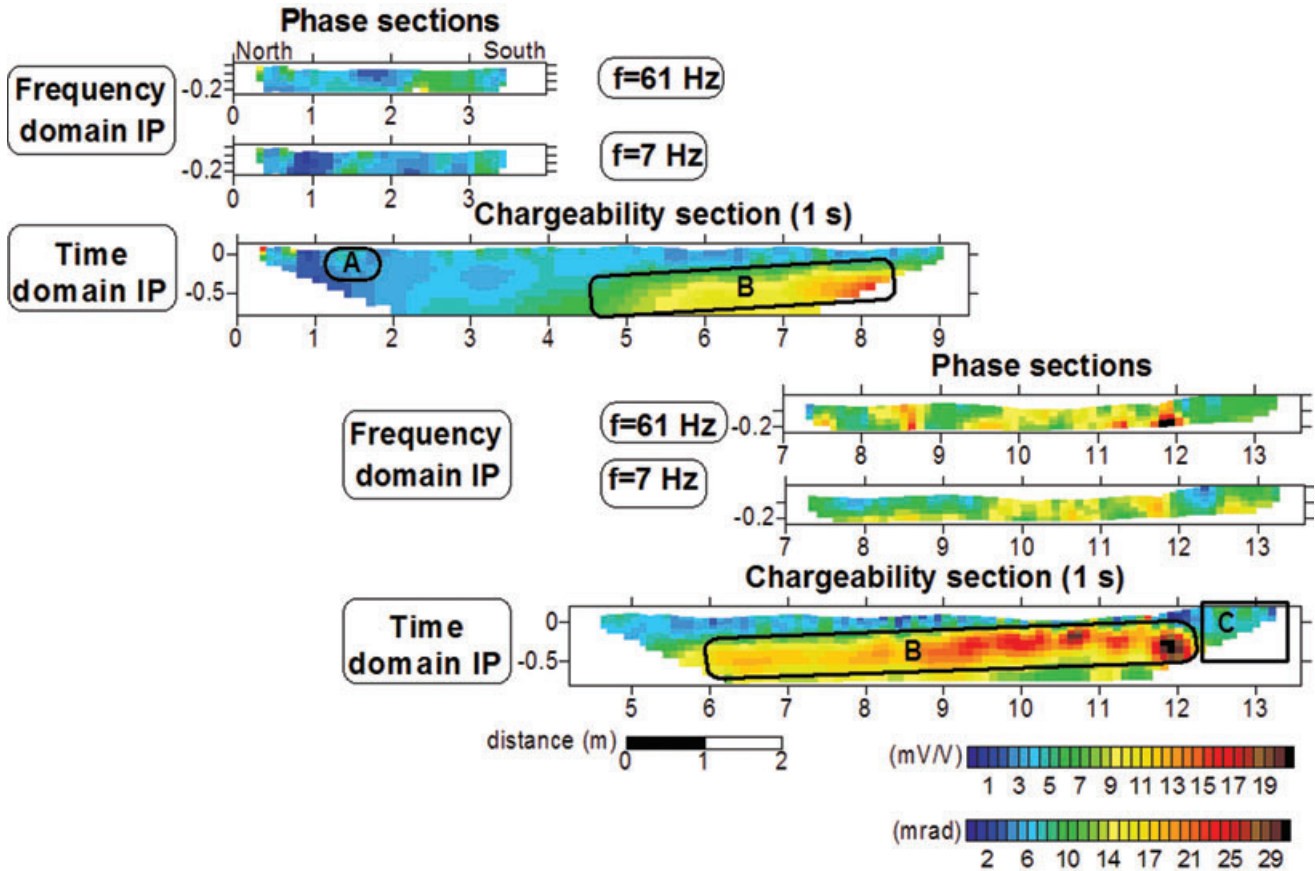


**Figure 10** Inverted time-domain chargeability and phase lag tomograms ( $f = 7$  Hz, 61 Hz, Wenner-Schlumberger array) in the North gallery. The area A corresponds to calcite-filled tectonic fractures, the area B corresponds to the calcareous nodule level, and the area C corresponds to the area where there is a concrete layer. The acquisition was performed in June 2009. The errors are smaller than 1%. Inversion of the phase tomography for SIP Profile 1 (see Figure 4b) has been carried with 40 data points while we used 69 data points concerning the SIP Profile 2 (see Figure 4b). (Iteration number: 4). The choice of the two frequencies represent a trade-off between the duration of the acquisition and the need to show low-frequency data for which there is a distinct polarization associated with the presence of the fractures. The phase section at 61 Hz shows an anomaly between 8 and 9 m that is not visible in the chargeability section. The origin of this anomaly is unclear and could be due to a local spurious electromagnetic coupling effect.

In the North gallery, a tectonic fracture intersects the beginning of the profile at 1.5 m (Fig. 3d). The signature of this tectonic fracture is hardly visible because of the higher dominant chargeability anomalies starting from 5 m from the beginning of the profile. According to the observations made during the excavation of the gallery, calcareous nodules were observed in this area (around  $x = 5$  m in Fig. 10). The size of these calcareous nodules is  $\sim 10$  cm long and  $\sim 20$  cm wide (Fig. 3c). We cannot see these nodules on the resistivity tomogram because the contrast in resistivity between these nodules and the matrix in which they are embedded is too low (Fig. 9).

Figure 11 shows the spectra of frequency data concerning the measurement along the floor, at the calcareous nodule level and at the clay-concrete interface, respectively. We do

not observe an IP signature similar to what was observed with the tectonic fractures in the East gallery (see above). In order to understand the origin of the strong chargeability associated with the calcareous nodule, we performed again a mineralogical analyse using a sample of the nodule from the floor of this gallery. The X-ray diffraction analysis indicates a weight fraction of 5–6% of pyrite.

## 5 DISCUSSION

### 5.1 Influence of water saturation

The influence of water saturation was discussed in detail in some of our previous publications (Cosenza *et al.* 2007;

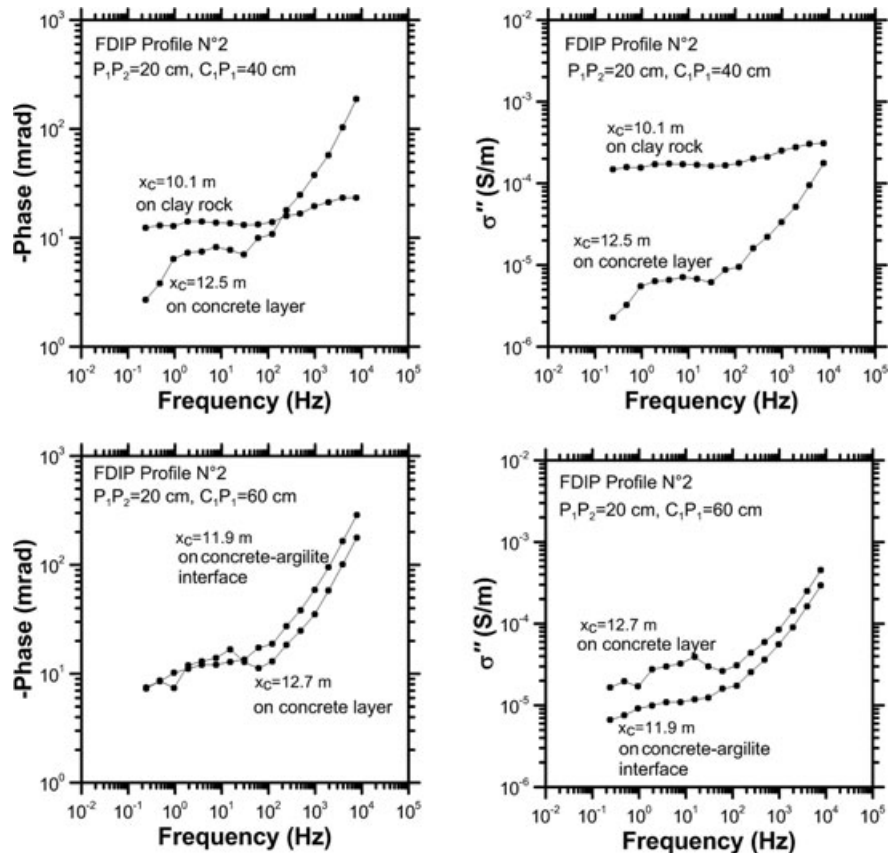


Figure 11 Phase lag and quadrature conductivity spectra along the longitudinal profile on the floor of the North gallery on clay rock and on concrete layer (FDIP Profile N°2, Wenner-Schlumberger array, distance between potential electrodes: 20 cm and distance between potential-current electrodes: 40 cm, 60 cm prototype from the Sisyph Laboratory, Paris, France).

Ghorbani *et al.* 2009; Jougnot *et al.* 2010). Figure 12 shows the effect of water saturation upon both the magnitude of the resistivity and the phase from laboratory experiments using a clay-rock sample from the Callovo-Oxfordian clay-rock from the Paris Basin (France). As expected the resistivity increases with the decrease of the water saturation and therefore this explains why the resistivity tomograms are good indicators of the extension of the damaged zone (Fig. 16). The magnitude of the phase also increases with the decrease of the water saturation because it is proportional to the resistivity. This data set was fairly well-reproduced from the model developed by Jougnot *et al.* (2010) based on combining the Stern layer and Maxwell-Wagner polarization models.

## 5.2 Influence of fractures

The influence of the freshly formed cracks filled with air upon the polarization is sketched in Fig. 14. The presence of these

air-filled fractures increases drastically the time constant in the so-called heating phase (see Fig. 13a) and therefore the peak of the low-frequency polarization is happening at lower frequencies. However this laboratory observation is hardly observed in the field as the open cracks are not associated with high chargeability. This may be because the increase of the chargeability associated with the decrease of the water saturation is partly counterbalanced by the decrease of the chargeability associated with the air-filled cracks.

The physical origin of the decrease of chargeability associated with a high density of air-filled cracks is still unclear at this stage. A simple explanation could be proposed with regard to the isolating nature of these fractures. Indeed, these air-filled fractures would act as effective barriers to the flow of the electrical current leading to some build-up of charges at their vertical surfaces. When the exiting current is stopped, some small and slow back-diffusion currents would occur in the opposite direction leading macroscopically to decrease the

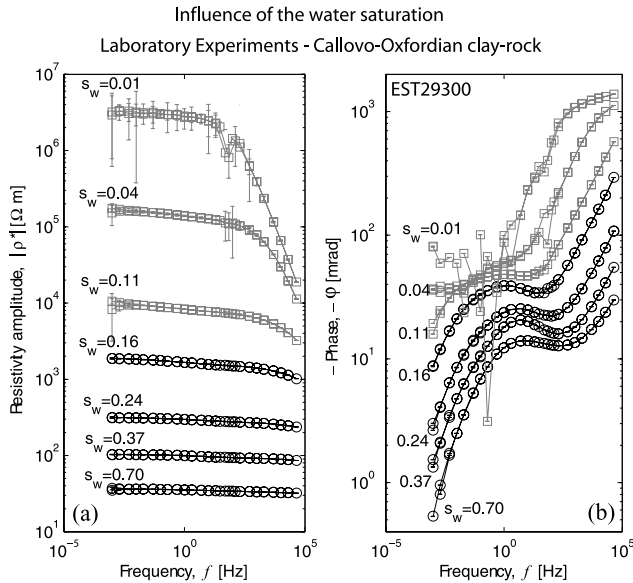


**Figure 12** Experimental spectral induced polarization data (sample 871 EST29300 from the Callovo-Oxfordian formation of the Paris Basin) at seven different saturations of the water phase  $s_w$  and for the frequency range 1 mHz – 45 kHz. a) Amplitude of the resistivity versus the frequency. Note the strong increase of the resistivity with the decrease of the water saturation. b) Phase versus frequency. The black open circles represent the data obtained during the desaturation phase by drying the sample at ambient temperature (values of the water saturations:  $s_w = 0.70, 0.37, 0.24,$  and  $0.16$ ). The grey open squares correspond to the heating phase where the water saturation was further decreased by heating the sample and then cooling it down to ambient temperature to perform the frequency-domain induced polarization measurements ( $s_w = 0.11, 0.04,$  and  $0.01$ ). The lines are just guides for the eyes (modified from Jougnot *et al.*, 2010). The low-frequency dispersion may be associated with the presence of pyrite while the high frequency behaviour in  $i\omega\varepsilon_\infty$  ( $\varepsilon_\infty$  being the high frequency dielectric constant) is expected from the theory (see Vinegar and Waxman, 1984).

apparent polarizability of the clay-rock. This geometric effect could be checked by numerical modelling, which should also account explicitly for the IP effect related to the desaturation of the clay matrix. Indeed, in order to provide some physical insights, a phenomenological approach based on experimental investigations in the laboratory seems unrealistic in this context because of the dimensions and the spatial organization of these air-filled cracks.

### 5.3 Influence of pyrite

Pelton *et al.* (1978) used the experimental data obtained by Chr. Grisseman for his PhD thesis at Innsbruck University (Austria) using artificial mixtures of sulphides, quartz and ce-

ment to investigate the role of pyrite on the frequency domain IP response. The spectra were acquired in a frequency range of 4 Hz to 10 kHz, above the frequency for which we observed a polarization effect. As discussed by Pelton *et al.* (1978), the presence of pyrite affects the induced polarization properties of a porous material. Both the grain size of the pyrite crystals (more precisely the square of their grain size) and the concentration of pyrite have a strong influence on the apparent time constant observed in induced polarization (Fig. 15).

In our case, both the concentration (in the range 6–8% in volume) and the grain size (between 0.1–1 mm) can be used to predict the range of time constants of the Cole-Cole response. From Fig. 15(c), we obtain a time constant in the range 0.03 s to  $3.2 \times 10^{-3}$  s and an intrinsic chargeability of 0.4. In the Cole-Cole model the peak frequency is related to the time constant  $\tau$  by,

$$f_c = \frac{1}{2\pi\tau(1-m)^{1/2c}}, \quad (3)$$

where  $m$  is the intrinsic chargeability and  $c$  the Cole-Cole exponent. It follows that the peak frequency is comprised between 12–120 Hz with  $m = 0.4$  (see Fig. 15) and  $c = 0.3$  (Fig. 13a), so above the observed low-frequency relaxation, which is always below 1 Hz (see Fig. 7). The low-frequency behaviour ( $<1$  Hz) was not investigated by Chr. Grisseman. Other investigations of natural ore samples (e.g., Marshall and Madden 1959) show that ore particles with a diameter of less than 1 mm can be responsible for phase peaks at frequencies below 1 Hz (see Fig. 7). In the case of natural ores, the whole ore aggregate (e.g., the presence of veins) has to be considered and not the size of a single ore grain. So it is likely that the observed relaxation is associated with the presence of pyrite. In turn, this implies however that frequency domain induced polarization performed at few tens to few hundred Hertz is suited to observe these calcite-filled fractures because of the presence of pyrite (see Table 1).

## 6 CONCLUSION

We studied the relationship between the presence of macroscopic heterogeneities in the Toarcian clay-rock formation of the Tournemire test site (Aveyron, France) using both time-domain and frequency domain induced polarization measurements. Three types of heterogeneities are observed: tectonic fractures, new cracks (associated with the excavation of the galleries) and calcareous nodules.

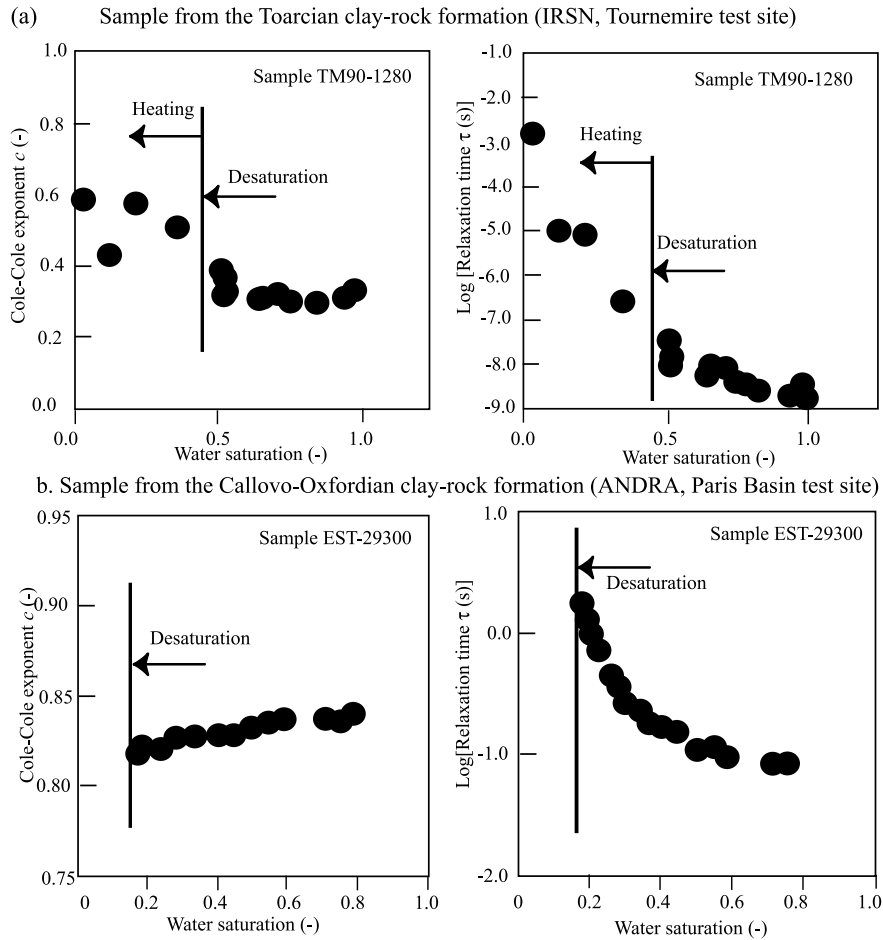


**Figure 13** Effect of the saturation upon the Cole-Cole exponent and the apparent time constant determined from frequency-domain induced polarization data. Modified from Cosenza *et al.* (2007) and Jougnot *et al.* (2010). Note the consistent increase by one order of magnitude of the time constant in the desaturation phase (no microcracks present). In the heating phase, the presence of microcracks has a strong influence on the Cole-Cole exponent and the time constant.

The IP signature of the calcite-filled tectonic fractures is potentially associated to their mineralization because of the presence of pyrite in the filling material. A relaxation is observed below 1 Hz in the phase and imaginary conductivity spectra of the calcite-filled tectonic fracture levels. This observation is consistently made using different types of arrays and electrode spacing. The pyrite itself seems however to produce some polarization at few tens to few hundreds of Hz.

The new cracks (observed by visual inspection along the gallery floors) control the change in the water content (desaturation) of the clay-rock in the damaged zone surrounding the galleries. They are associated with low chargeabilities ( $\leq 4$  mV/V). This response is almost in the same order of magnitude as the intrinsic IP response of the clay-rock matrix

itself. This implies that these features may be difficult to see on the tomograms. We observed that a gallery like the East gallery excavated a long time ago (in 1996) presents however lower chargeability values than the more recently excavated gallery (North gallery, excavated in 2008). This observation may be associated to the much longer exposition time of the older gallery (excavated in 1996) to the desaturation from the new fractures (smaller water contents due to the desaturation are associated with lower chargeabilities).

With the resistivity tomograms alone, it is difficult to distinguish between the tectonic fractures and the new cracks associated with the excavation of the galleries. However, the extension of the damaged zone is clearly visible because of the overall change in water saturation with respect to the fully,

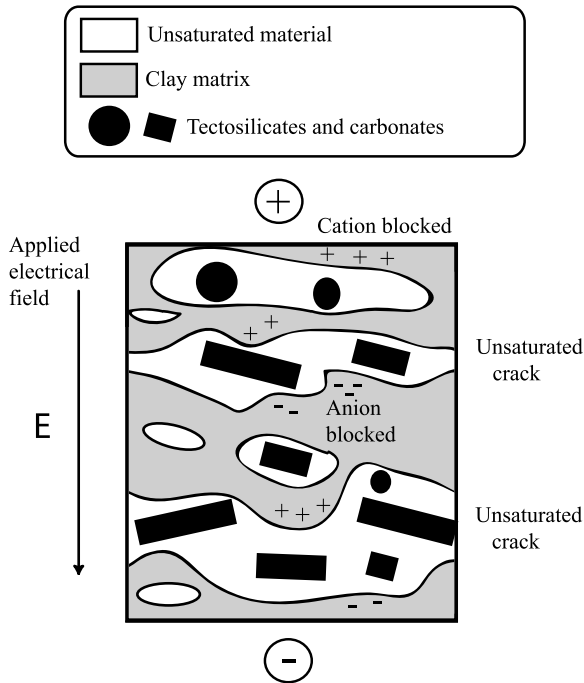


**Figure 14** Possible influence of the new fractures on the polarization response. The new fractures filled with air are responsible for an increasing of the blocking of the ions during their electromigration. The effect is substantial in the direction normal to the position of the cracks. Modified from Cosenza *et al.* (2007).

undamaged, clay-rock. The resistivity tomogram shows that the damaged zone thickness of the North gallery, excavated in 2008, is less important (<50 cm) compared to the excavation damaged zone thickness of the East gallery excavated in 1996 (50–80 cm).

Finally, the calcareous nodules embedded in some areas in the clay-rock matrix are associated with high chargeabilities. According to our X-ray analysis, the mineralization of these nodules has 5–6% pyrite in weight. This pyrite may explain the observed IP response. The Maxwell-Wagner may also play a role. The contrast in the resistivity is not high enough to detect the presence of these calcareous nodules showing once more the complementarity between resistivity and induced polarization.

Future directions will be to monitor jointly seismic and complex conductivity of the damaged zone to see through time-lapse joint inversion how the properties of the excavation damaged zone may change with time. It will also be necessary to account for the full tensorial nature of the material properties (complex resistivity and stiffness tensors) associated with

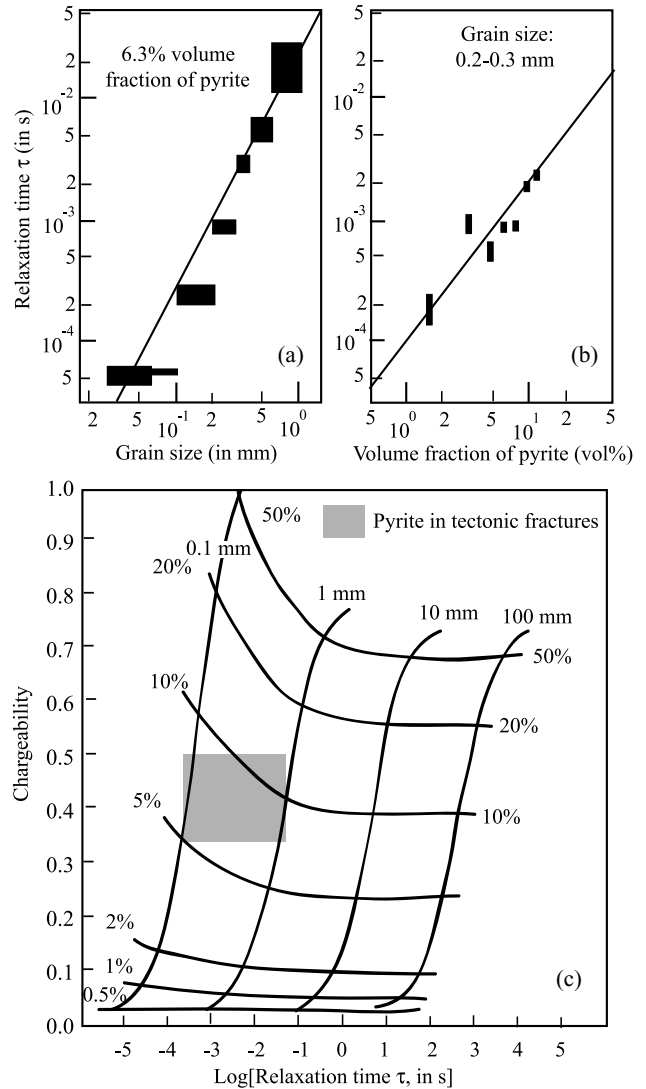


**Figure 15** Possible influence of the pyrite grains located in the calcite-filled tectonic fractures. a) b) Determination of the time constant by Pelton *et al.* (1978). Note that the time constant depends on the square of the diameter of the pyrite grains. c) Chargeability and time constant as a function of the grain size of pyrite and its volumetric fraction (modified from Pelton *et al.*, 1978). Veins of pyrite can produce a polarization at lower frequencies.

the anisotropic behaviour of the material associated with the presence of the fractures.

**ACKNOWLEDGEMENTS**

This research was supported by The French Institute for Radioprotection and Nuclear Safety (IRSN) and, in its initial phase, by the Agence Nationale de la Recherche

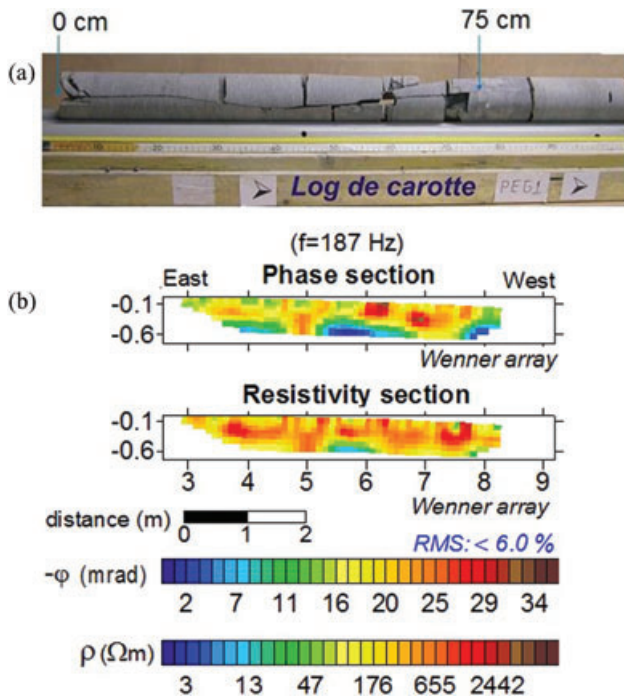


**Figure 16** Influence of the desaturation of the clay-rock. a) Extracted clay sample at a new fracture observed on the floor of the East gallery ( $x = 1$  m). This partially air-saturated new fractures propagate in depth (to a depth of 75 cm from the gallery walls as shown by the fracture along the axis of the core sample). Such fractures probably control the desaturation of clay-rock matrix in the EDZ. b) Inverted resistivity and phase from frequency-domain IP data (at  $f = 187$  Hz, Wenner array, iteration number: 4, East gallery). The acquisition were performed in June 2008. The data shows a high resistivity and a high magnitude of the phase because of the effect of the drying.

(ANR) – ECCO program (POLARIS Project: ‘Polarisation Provoquée Spectrale’ – Spectral Induced Polarization). The authors are grateful to Pauline Kessouri, Claude Fontaine at Poitiers University for carrying out the X-ray diffraction analysis and to Sebastien Flageul at Pierre Marie Curie University for providing the prototype measurement device and for his help. A. Revil thanks DOE (BER, DE-FG02-08ER646559). We thank the Associate Editor, Oliver Ritter, for the speed and quality of the review process, Andreas Hördt and an anonymous referee for their constructive reviews. The second anonymous referee provided very useful information concerning the work of Chr. Grisseman, which is discussed in Pelton *et al.* (1978).

## REFERENCES

Binley A., Slater L.D., Fukes M. and Cassiani G. 2005. Relationship between spectral induced polarization and hydraulic properties of

saturated and unsaturated sandstones. *Water Resource Research* 41, W12417. doi:10.1029/2005WR004202

Blümling P., Bernier F., Lebon P. and Derek Martin C. 2007. Excavation damaged zone in clay formations time-dependent behaviour and influence on performance assessment. *Physics and Chemistry of the Earth* 32, 588–599.

Boisson J.Y., Cabrera J. and De Windt L. 1996. Investigating faults and fractures in argillaceous Toarcian formation at the IPSN Tournemire research site. Joint OECD/NEA-EC Workshop on Fluid Flow through Faults and Fractures in Argillaceous Formation, Bern, Switzerland, Expanded Abstracts, 207–222.

Boisson J.Y., Cabrera J. and De Windt L. 1997. Caractérisation d’une formation argileuse-Caractérisation des propriétés de transferts au laboratoire des argilites et marnes toarciennes de Tournemire, Aveyron, France. CCE report no. 5, ref. SERGD 97/04.

Bonin B. 1998. Deep geological disposal in argillaceous formations: Studies at the Tournemire test site. *Journal Contamination Hydrology* 35, 315–330.

Börner F.D., Schopper J.R. and Weller A. 1996. Evaluation of transport and storage properties in the soil and groundwater zone from induced polarization measurements. *Geophysical Prospecting* 44, 583–602.

Bossart P., Meier P., Moeri A., Trick T. and Mayor J. 2002. Geological and hydraulic characterisation of the excavation disturbed zone in the Opalinus Clay of the Mont Terri Rock Laboratory. *Engineering Geology* 66, 19–38.

Cabrera J., Beaucaire C., Bruno G., De Windt L., Genty A., Ramambaso N. *et al.* 2001. Projet Tournemire – Synthèse des programmes de recherche 1995–1999. Report #IPSN DP/RE/SERGD 01–19, Paris, France.

Campbell D.L., Horton R.J. and Beanlang S. 2000. Geoelectrical laboratory measurements of materials from the May Say mine dump, Southwestern Colorado. Open-File Report 00–382, USGS, 27 p.

Contrucci L., Cabrera J., Klein E. and Ben-Slimane K. 2007. EDZ investigations by ultrasonic borehole logging in drifts of different ages excavated in argillaceous formations of the Tournemire experimental station. Annual International Meeting, ANDRA, Clays in Natural and Engineered Barriers for Radioactive Waste Confinement, 17–18 September, Lille, France, Expanded Abstracts.

Cosenza P., Ghorbani A., Florsch N. and Revil A. 2007. Effects of drying on the low frequency electrical properties of Tournemire argillites. *Pure and Applied Geophysics* 164, 2043–2066. doi:10.1007/s00024-007-0253-0

Cosenza P., Ghorbani A., Revil A., Zamora M., Schmutz M., Jougnot D. and Florsch N. 2008. A physical model of the low-frequency electrical polarization of clay-rocks. *Journal of Geophysical Research* 113, B08204. doi:10.1029/2007JB005539

Dahlin T., Leroux V. and Nissen J. 2002. Measuring techniques in induced polarisation imaging. *Journal of Applied Geophysics* 50, 279–298.

De Groot Hedlin C. 1990. Occam’s inversion to generate smooth, two dimensional models from magnetotelluric data. *Geophysics* 55, 1613–1624

De Windt L., Cabrera J. and Boisson J.Y. 1999. Radioactive waste containment in indurated shales: Comparison between the

- chemical containment properties of matrix and fractures. In: *Chemical Containment of Waste in the Geosphere* (eds R. Metcalfe and C.A. Rochelle), 167–181.
- Gélis C., Revil A., Cushing M.E., Jougnot D., Lemeille F., Cabrera J. et al. 2010. Potential of electrical resistivity tomography to detect fault zones in limestone and argillaceous formations in the experimental site of Tournemire, France. *Pure and Applied Geophysics* 167, 1405–1418. doi:10.1007/s00024-010-0097-x
- Ghorbani A., Camerlynck C., Florsch N., Cosenza P., Tabbagh A. and Revil A. 2007. Bayesian inference of the Cole-Cole parameters from time and frequency-domain induced polarization. *Geophysical Prospecting* 55, 589–605. doi:10.1111/j.1365-2478.2007.00627.x
- Ghorbani A., Cosenza P., Revil A., Zamora M., Schmutz M., Florsch N. and Jougnot D. 2009. Non-invasive monitoring of water content and textural changes in clay-rocks using spectral induced polarization: A laboratory investigation. *Applied Clay Science* 43, 493–502. doi:10.1016/j.clay.2008.12.007
- Jougnot D., Ghorbani A., Revil A., Leroy P. and Cosenza P. 2010. Spectral induced polarization of partially saturated clay-rocks: A mechanistic approach. *Geophysical Journal International* 180, 210–224. doi:10.1111/j.1365-246X.2009.04426.x
- Karaoulis M., Revil A., Werkema D.D., Minsley B., Woodruff W.F. and Kemna A. 2011. Time-lapse 3D inversion of complex conductivity data using an active time constrained (ATC) approach. *Geophysical Journal International*. doi:10.1111/j.1365-246X.2011.05156.x
- Kemna A. 2000. *Tomographic inversion of complex resistivity: Theory and application*. PhD thesis, Bochum University.
- Kemna A., Binley A. and Slater L. 2004. Cross-borehole IP imaging for engineering and environmental applications. *Geophysics* 69, 97–105.
- Kenkel J., Hördt A. and Kemna A. 2011. 2D modelling of induced polarisation data with anisotropic resistivities. *Near Surface Geophysics* (submitted).
- Knight R.J. and Endres A. 1990. A new concept in modelling the dielectric response of sandstones. *Geophysics* 55, 586–594.
- Kruschwitz S. and Yaramanci U. 2004. Detection and characterization of the disturbed rock zone in claystone with complex resistivity method. *Journal of Applied Geophysics* 57, 63–79. doi:10.1016/j.jappgeo.2004.09.003
- Leroy P. and Revil A. 2009. Spectral induced polarization of clays and clay-rocks. *Journal of Geophysical Research* 114, B10202. doi:10.1029/2008JB006114
- Leroy P., Revil A., Kemna A., Cosenza P. and Ghorbani A. 2008. Spectral induced polarization of water-saturated packs of glass beads. *Journal of Colloid and Interface Science* 321, 103–117.
- Lesmes D.P. and Friedman S.P. 2005. Relationships between the electrical and hydrogeological properties of rocks and soils. In: *Hydrogeophysics* (eds Y. Rubin and S.S. Hubbard), pp. 87–128. Springer.
- Lesmes D.P. and Frye K.M. 2001. The influence of pore fluid chemistry on the complex conductivity and induced polarization responses of Berea sandstone. *Journal of Geophysical Research* 106, 4079–4090
- Loke M.H. and Barker R.D. 1996. Rapid least-squares inversion of apparent resistivity pseudo sections using a quasi-Newton method. *Geophysical Prospecting* 44, 131–152.
- Marshall D.J. and Madden T.R. 1959. Induced polarization: A study of its causes. *Geophysics* 24, 790–816. doi:10.1190/1.1438659
- Mathieu R., Pagel M., Clauer N., De Windt L., Cabrera J. and Boisson J.Y. 2000. Paleofluid circulations records in shales: A mineralogical and geochemical study of calcite veins from the experimental Tournemire tunnel site. *European Journal of Mineralogy* 12, 377–390.
- Matray J.M., Savoye S. and Cabrera J. 2007. Desaturation and structure relationships around drifts excavated in the well-compacted Tournemire's argillite. *Engineering Geology* 90, 1–16.
- Nelson P.H. and Van Voorhis G.D. 1973. Letter to the editor regarding the paper "Complex resistivity spectra of porphyry copper mineralization". *Geophysics* 38, 984.
- Nelson P.H. and Van Voorhis G.D. 1983. Estimation of sulphide content from induced polarisation data. *Geophysics* 48, 62–76.
- Nover G., Heikamp S. and Freund D. 2000. Electrical impedance spectroscopy used as a tool for the detection of fractures in rock samples exposed to either hydrostatic or triaxial pressure conditions. *Natural Hazards* 21, 317–330.
- Olhoeft G.R. 1984. Clay-organic interactions measured with complex resistivity. 54<sup>th</sup> SEG meeting, Atlanta, Georgia, USA, Expanded Abstracts, 356–358.
- Olhoeft G.R. 1985. Low-frequency electrical properties. *Geophysics* 50, 2492–2503.
- Olhoeft G.R. 1992. Geophysical detection of hydrocarbon and organic chemical contamination. *Proceedings of the Symposium on the Application of Geophysics to Engineering and Environmental Problems*, Expanded Abstracts, 587–594.
- Pelton W.H., Sill W.R. and Smith B.D. 1983. Interpretation of complex resistivity and dielectric data, part I. *Geophysical Transactions* 29, 297–330.
- Pelton W.H., Ward S.H., Hallof P.G., Sill W.R. and Nelson P.H. 1978. Mineral discrimination and removal of inductive coupling with multifrequency IP. *Geophysics* 43, 588–609.
- Peyaud J.B., Pagel M., Cabrera J. and Pitsch H. 2006. Mineralogical, chemical and isotopic perturbations induced in shale by fluid circulation in a fault at the Tournemire experimental site (Aveyron, France). *Journal of Geochemical Exploration* 90, 9–23.
- Rejeb A. and Cabrera J. 2006. Time-dependent evolution of the excavation damaged zone in the argillaceous Tournemire site. The GeoProc International Conference on Coupled T-H-M-C Processes in Geosystems: Fundamentals, Modelling, Experiments and Applications (invited lecture), 22–25 May, Nanjing, China.
- Revil A. and Florsch N. 2010. Determination of permeability from spectral induced polarization data in granular media. *Geophysical Journal International* 181, 1480–1498. doi:10.1111/j.1365-246X.2010.04573.x
- Savoye S., Michelot J.L., Wittebroodt C. and Altinier M.V. 2006. Contribution of the diffusive exchange method to the characterization of pore-water in consolidated argillaceous rocks. *Journal of Contaminant Hydrology* 86, 87–104.
- Savoye S., De Windt L., Beaucaire C., Bruno G. and Guitard N. 2001. Are artificial tracers conservative in argillaceous media? The

- Tournemire claystone case. *Water Rock Interaction Proceedings* 10, 1383–1386.
- Schmutz M., Ghorbani A., Vaudelet P. and Revil A. 2011. Spectral IP detects cracks and distinguishes between open and clay-filled fractures. *Journal of Environmental and Engineering Geophysics* 16, 85–91.
- Schmutz M., Revil A., Vaudelet P., Batzle M., Femenía Viñao P. and Werkema D.D. 2010. Influence of oil saturation upon spectral induced polarization of oil bearing sands. *Geophysical Journal International* 183, 211–224. doi:10.1111/j.1365-246X.2010.04751.x
- Schwartz L.M., Sen P.N. and Johnson D.L. 1989. Influence of rough surfaces on electrolytic conduction. *Physics Review B* 40, 2450–2458.
- Seigel H., Nabighian M., Parasnis D.S. and Vozoff K. 2007. The early history of the induced polarization method. *The Leading Edge* 3, 312–321.
- Sen P.N., Chew W.C. and Wilkinson D. 1984. Dielectric enhancement due to geometrical and electrochemical effects. In: *Physics and Chemistry of Porous Media* (eds D.L. Johnson and P.N. Sen), pp. 52–65. American Institute of Physics.
- Slater L. and Lesmes D.P. 2002. IP Interpretation in environmental investigations. *Geophysics* 67, 77–88.
- Sturrock J.T., Lesmes D. and Morgan F.D. 1999. Permeability estimation using spectral induced polarization measurements. *Proceedings on the Symposium on the Application of Geophysics to Engineering and Environmental Problems*, Expanded Abstracts, 409–415.
- Tikhonov A.N. and Arsenin V.Y. 1977. *Solutions of Ill-posed Problems*. W.H. Winston.
- Tsang C., Bernier F. and Davies C. 2005. Geohydromechanical processes in the excavation damaged zone in crystalline rock, rock salt, and indurated and plastic clays in the context of radioactive waste disposal. *International Journal of Rock Mechanics and Mining Sciences* 42, 109–125.
- Van Voorhis G.D., Nelson P.H. and Drake T.L. 1973. Complex resistivity spectra of porphyry copper mineralization. *Geophysics* 38, 49–60.
- Vanhala H., Soininen H. and Kukkonen I. 1992. Detecting organic chemical contaminants by spectral-induced polarization method in glacial till environment. *Geophysics* 57, 1014–1017.
- Vaudelet P., Revil A., Schmutz M., Franceschi M. and Bégassat P. 2011a. Induced polarization signatures of cations exhibiting differential sorption behaviors in saturated sands. *Water Resource Research* 47, W02526. doi:10.1029/2010WR009310
- Vaudelet P., Revil A., Schmutz M., Franceschi M. and Bégassat P. 2011b. Changes in induced polarization associated with the sorption of sodium, lead, and zinc on silica sands. *Journal of Colloid and Interface Science*, 360, 739–752, 2011.
- Vauhkonen M., Vadász D., Karjalainen P., Somersalo E. and Kaipio J. 1998. Tikhonov regularization and prior information in electrical impedance tomography. *IEEE Transactions Medical Imaging* 17, 285–293.
- Vinegar H.J. and Waxman M.H. 1984. Induced polarization of shaly sands. *Geophysics* 49, 1267–1287.
- Weller A. and Börner F. 1996. Measurements of spectral induced polarization for environmental purposes. *Environmental Geology* 27, 329–334.
- Weller A., Seichter M. and Kampke A. 1996. Induced-polarization modelling using complex electrical conductivities. *Geophysical Journal International* 127, 387–398.
- Wong J. 1979. An electrochemical model of the induced-polarization phenomenon in disseminated sulphide ores. *Geophysics*, 44, 1245–1265.